Research Article

Coordination-driven self-assembly of metallo-nanodrugs for local inflammation alleviation

Lijuan Tang[1,2,3,§], Zhenghan Di[3,§], Jingfang Zhang[3], Feiying Yin[1], Lele Li[3] (✉), and Li Zheng[1] (✉)

[1] *Guangxi Key Laboratory of Regenerative Medicine, Guangxi Engineering Center in Biomedical Material for Tissue and Organ Regeneration, Collaborative Innovation Centre of Regenerative Medicine and Medical BioResource Development nd Application Co-Constructed by the Province and Ministry, The First Affiliated Hospital of Guangxi Medical University, Nanning 530021, China*

[2] *Pharmaceutical College, Guangxi Medical University, Nanning 530021, China*

[3] *CAS Key Laboratory for Biomedical Effects of Nanomaterials and Nanosafety, National Center for Nanoscience and Technology, Beijing 100190, China*

§ *Lijuan Tang and Zhenghan Di contributed equally to this work.*

ABSTRACT

Developing dedicated nanomedicines to improve delivery efficacy of anti-inflammatory drugs is still a formidable challenge. In this study, we present an extremely simple yet efficient approach to obtain hybrid nanodrugs through metal-drug coordination-driven self-assembly for carrier-free drug delivery. The resulting metallo-nanodrugs exhibit well-defined morphology and high drug encapsulation capability, allowing for the combination of magnetic resonance imaging and anti-inflammatory therapy. In the case of osteoarthritis (OA), the metallo-nanodrugs remarkably alleviate synovial inflammation, preventing cartilage destruction and extracellular matrix loss. In addition, it led to significantly improved therapeutic efficacy compared with intra-articular administration of the same dose of free drugs in OA mouse model. This work provides a very simple approach for the development of anti-inflammatory nanoformulations by exploiting coordination-driven self-assembly.

KEYWORDS

drug delivery, coordination-driven assembly, nanomedicine, anti-inflammation therapy

1   Introduction

Local inflammation is associated with a myriad of diseases, including atherosclerosis, neurodegenerative disease, and tumor [1]. Osteoarthritis (OA) is a chronic joint disorder accompanied by inflammation, which is typically characterized by progressive loss of cartilage, leading to impeding mobility, pain, and even disability in the elderly [2, 3]. Cartilage fragments or extracellular matrix (ECM) factors released during OA serve as damage-associated molecular patterns to induce inflammatory responses in synovial cells, which increase ECM degradation and perpetuate cartilage damage [3, 4]. Current treatment involves intra-articular administration of corticosteroids to palliate the pain symptoms and ameliorate inflammation [5, 6]. However, rapid clearance from the joint space poses formidable challenges for local delivery of anti-inflammatory agents [6, 7]. The short half-life of these agents and the requirement for repeated injections limited the therapeutic applications. Therefore, there is an unmet need for the development of strategies that enables efficient delivery and improved therapeutic efficacy.

The advancement in the field of nanotechnology affords myriads of approaches that can significantly improve the efficacy and safety of small molecule drugs [8, 9]. Coordination-driven self-assembly has emerged as a promising strategy for the construction of nanoscale delivery vehicles [10, 11]. An elegant example is coordination polymers (CPs) which are built via metal-ligand coordination bonds [11]. CPs have several advantages as nanocarriers such as structure tunability, high loading efficiency, and biocompatibility [12, 13]. The past decades have witnessed significant advancement in the development of cargo-incorporating CPs for biosensing, imaging, and therapy [12–19]. In particular, numerous CPs loaded with small molecule drugs during particle synthesis or through postsynthetic encapsulation have been reported for tumor treatment [20–29], which could improve the distribution specificity and pharmacokinetics properties of these therapeutics for enhanced therapeutic efficacy. Recently, our group has reported the synthesis of multifunctional nanostructures through coordination-driven assembly of Fe^{II} ions and DNA molecules, allowing for efficient transport of antitumor nucleic acids [30–32]. Most recently, the approach has been extended to the synthesis of metal-RNA hybrid nanostructures for therapeutic RNA delivery [33].

Inspired by these achievements, here we present a simple strategy for the synthesis of hybrid metallo-nanodrugs through coordination-mediated self-assembly of Fe^{II} ions and dexamethasone sodium phosphate (DexP) (Fig. 1(a)). Dexamethasone, a powerful corticosteroid, is widely used for anti-inflammatory therapy [34]. The obtained metallo-nanodrugs, referred to as Fe-DexP nanoparticles (NPs), are achieved via a one-step assembly of DexP and Fe^{II} ions to generate hybrid nanoparticles in high yield. In inflamed joints, Fe-DexP NPs could
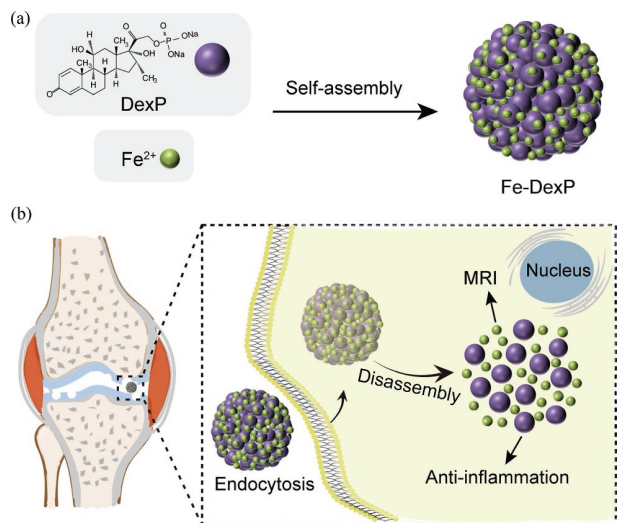

Figure 1 Schematic showing coordination-driven assembly of metallo-nanodrugs for OA alleviation. (a) One-pot synthesis of Fe-DexP NPs. (b) Use of Fe-DexP NPs for OA treatment.

be degraded gradually for sustained cargo release, enabling magnetic resonance imaging (MRI) and mitigating synovial inflammation to inhibit cartilage destruction (Fig. 1(b)). This strategy avoids the use of extra synthetic materials as drug vehicles, thereby allowing anti-inflammatory drugs to be delivered in a carrier-free manner with high efficiency.

2 Results and discussion

2.1 Preparation and characterization of Fe-DexP

As shown in Figs. 2(a)–2(c), the Fe-DexP NPs exhibited a spherical morphology with coarse surface. Dynamic light scattering (DLS) measurement showed that Fe-DexP NPs were negatively charged (-23.7 mV) with a hydrodynamic diameter of 107.9 ± 38.9 nm (Fig. 2(d)). P, O (from DexP), and Fe elements were evenly distributed in the NPs, as indicated by high-angle annular dark-field scanning transmission electron microscopy-energy-dispersive X-ray spectroscopy (HAADF-STEM-EDS) elemental mappings (Fig. 2(e)). The composition of the NPs was also confirmed by X-ray photoelectron spectroscopy (XPS) (Fig. 2(f)). As indicated in the high-resolution spectrum of Fe 2p, two peaks at 710.7 and 724.4 eV were assigned to Fe $2p_{3/2}$ and Fe $2p_{1/2}$ peaks, respectively (Fig. 2(g)) [35]. The molar ratio of Fe^{3+}/Fe^{2+} is estimated to be 1.7:1. Magnetic property test revealed that the value of inverse relaxation time ($1/T_2$) of Fe-DexP NPs was positively correlated with the concentration of Fe, with the transverse relativity (r_2) calculated to be 41.2 $mM^{-1}\cdot s^{-1}$ (Fig. 2(h)). In addition, concentration-dependent signal increase was observed in T_2-weighted phantom images (inset in Fig. 2(h)), demonstrating the potential of Fe-DexP NPs as a MRI contrast agent. It's noteworthy that the synthesis of the NPs could be precisely controlled by adjusting reaction conditions. When Fe:DexP molar ratio was fixed at 2:1, the NPs exhibited gradually increased average diameter from 113.3 ± 31.1 to 184.7 ± 27.1 nm with the increase in the concentrations of reactants, while remaining spherical in morphology and uniform in size (Fig. S1 in the Electronic Supplementary Material (ESM)). The absence of DexP led to aggregated particles (Fig. S2 in the ESM), suggesting the critical role of DexP in NPs synthesis. The self-assembly strategy allows effective encapsulation of DexP with loading content and efficiency of 49.3% and 38.6%, respectively. Of note, many nanocarriers have been developed for the delivery of dexamethasone [36, 37], while the Fe-DexP NPs possessed a higher drug loading content in comparison with these systems. Next, the stability of Fe-DexP NPs was investigated in phosphate buffered solution (PBS) (pH 6.5) at 37 °C. TEM images showed that the NPs disassembled gradually and complete degradation was observed after 4 days (Fig. S3 in the ESM). The disassembly of
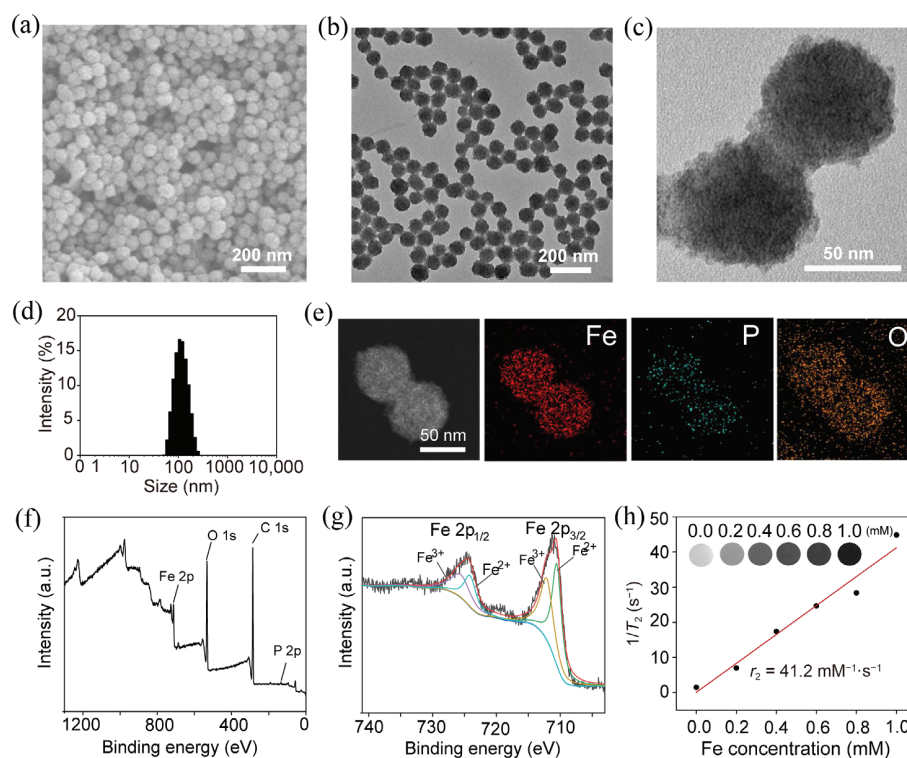

Figure 2 Characterization of Fe-DexP. ((a)–(c)) SEM (a) and TEM images ((b) and (c)) of Fe-DexP NPs. (d) Hydrodynamic size distribution of Fe-DexP NPs. (e) HAADF-STEM image of Fe-DexP NPs, along with the corresponding element maps for P, O, and Fe. ((f) and (g)) XPS survey spectrum (f) and high-resolution Fe 2p XPS spectrum (g) of Fe-DexP NPs. (h) Transverse relaxation rate ($1/T_2$) as a function of Fe concentration (inset: T_2-weighted MR images of Fe-DexP NPs at indicated Fe concentrations).

the Fe-DexP NPs was due to the weakened metal-DexP coordination interaction caused by the competitive interactions of metal ions with other molecules (e.g., phosphate ions), which is consistent with the previously reported mechanism for the drug release from the metal–organic nanostructures [38]. Furthermore, DexP could assemble with other metal ions (e.g., Mn^{II} ions) to form spherical nanostructures (Fig. S4 in the ESM), suggesting the universality of the approach.

2.2 *In vitro* anti-inflammatory activity of Fe-DexP

The biological activity of the system was assessed using lipopolysaccharide (LPS)-treated macrophages (RAW264.7), which showed elevated levels of pro-inflammatory cytokines [39, 40]. LPS-treated RAW264.7 cells were incubated with Fe-DexP NPs, followed by collection of the supernatant for the detection of IL-6 and TNF-α via enzyme-linked immunosorbent assay (ELISA). It showed that the elevated levels of the pro-inflammatory cytokines (IL-6 and TNF-α) by LPS treatment were effectively suppressed by Fe-DexP NPs (Figs. 3(a) and 3(b)). In addition, the inhibition capability of Fe-DexP NPs on cytokine secretion was concentration dependent (Fig. S5 in the ESM). This indicated that the anti-inflammatory activity of DexP was retained after assembly in NPs. Furthermore, ignorable cytotoxicity of the NPs to RAW264.7 cells was observed (Fig. 3(c)), suggesting the good biocompatibility of the system.

Since cyclooxygenase (COX)-2 is critically involved in inflammation progression [41, 42], regulation of COX-2 expression by Fe-DexP was examined by western blot. As expected, treatment with Fe-DexP NPs dramatically decreased COX-2 level for the LPS-treated macrophages (Fig. 3(d)). It is known that reactive oxygen specie (ROS) plays a vital role in inducing inflammatory-associated pathways [43], intracellular ROS production was thus interrogated with 2,7-dichlorofluorescein-diacetate (DCFH-DA). LPS induced the overproduction of ROS in RAW264.7 cells, as evidenced by obviously stronger intracellular fluorescence compared with the pristine ones (Fig. 3(e)). Treatment with Fe-DexP NPs led to dramatic reduction of the fluorescence signal in RAW264.7 cells (pre-induced by LPS) (Fig. 3(e)), manifesting its effect in ROS scavenging. Moreover, the ROS attenuation ability of Fe-DexP NPs was dose-dependent (Fig. S6 in the ESM). Quantitative results from flow cytometry analysis further verified the ability of Fe-DexP NPs to reduce excess ROS generation (Fig. 3(f)).

2.3 Fe-DexP repolarizes macrophages to inhibit chondrocyte death

Macrophages have been reported to play an important role in OA, with M1 macrophages secreting pro-inflammatory mediators and M2 macrophages producing anti-inflammatory cytokines [44, 45]. Thus, classic M1 and M2 markers were analyzed by quantitative real-time polymerase chain reaction (q-PCR) after Fe-DexP treatment. As depicted in Fig. 4(a), Fe-DexP NPs treatment significantly down-regulated the expression of iNOS and IL-12 (M1 markers) in RAW264.7 cells activated by LPS, demonstrating that Fe-DexP NPs could suppress M1 macrophage polarization. In contrast, expressions of Arg-1 and IL-10 (M2 markers) were up-regulated in the LPS + Fe-DexP NPs group compared with the LPS group (Fig. 4(b)), manifesting that Fe-DexP NPs facilitated anti-inflammatory M2 polarization. Considering that the inflammatory mediators released by macrophage can trigger apoptosis and necrosis of chondrocytes during OA progression [46, 47], we investigated the capability of Fe-DexP NPs to prohibit inflammation-mediated death of primary chondrocyte. Chondrocytes were incubated with the conditioned medium (CM) of RAW264.7 cells that underwent distinct treatments, followed by Cell Counting Kit-8 (CCK-8) assay. LPS activation resulted in strikingly enhanced cytotoxicity of CM, which was significantly weakened by further treatment with Fe-DexP NPs (Fig. 4(c)). Live/dead cell staining showed remarkable dead cells (red) referred by PI-positive cells in the LPS group, while an increase in the percentage of live chondrocytes (Calcein AM-positive cells, green) was observed in the LPS + Fe-DexP group
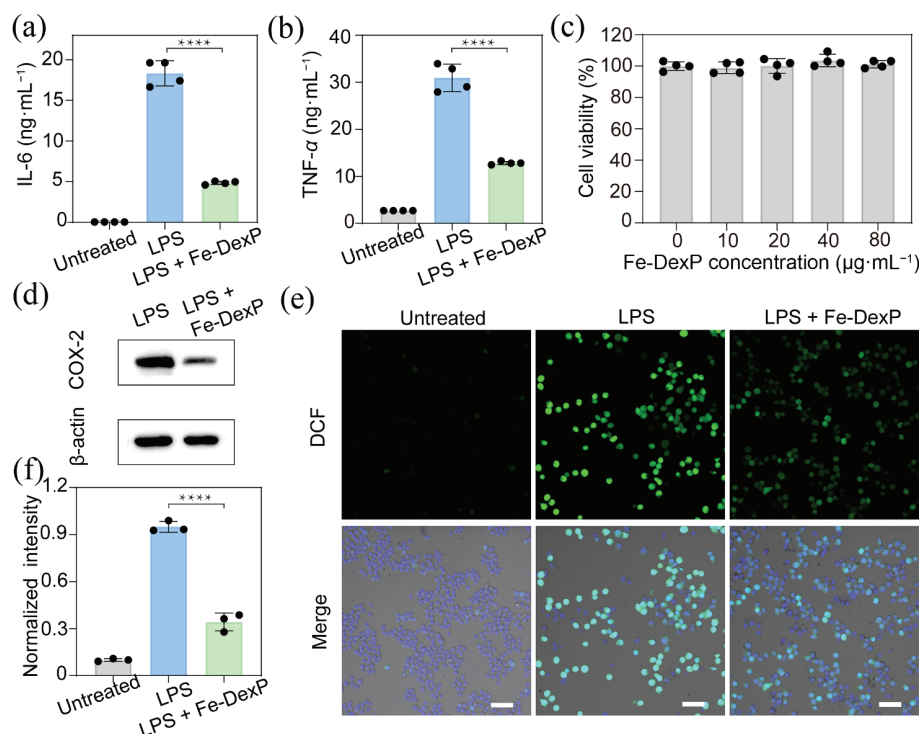

Figure 3 Anti-inflammatory effect of Fe-DexP. ((a) and (b)) Secretion of IL-6 (a) and TNF-α (b) by RAW264.7 cells with indicated treatments. (c) Cell viability of RAW264.7 cells exposed to different concentrations of Fe-DexP. (d) Western blot analysis of COX-2 protein levels in RAW264.7 cells with different treatments. β-actin serves as the loading control. ((e) and (f)) Representative fluorescence images (e) and flow cytometry analysis (f) of ROS levels in RAW264.7 cells after different treatments (scale bars, 200 μm; data are means ± SD, $n = 4$ (for (a)–(c)) and $n = 3$ (for (f)); ****$P < 0.0001$).
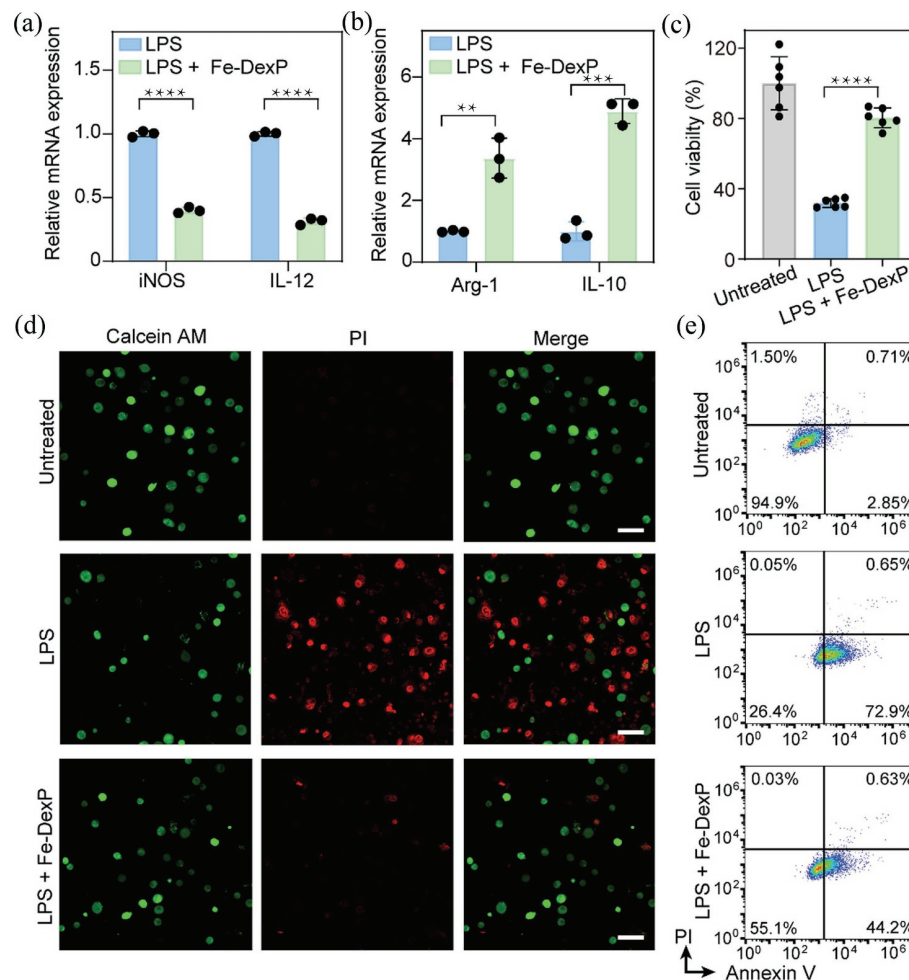
Figure 4 Fe-DexP facilitates macrophage polarization for chondrocyte death inhibition. ((a) and (b)) Expression of iNOS and IL-12 (M1 markers) (a) and Arg-1 and IL-10 (M2 markers) (b) in RAW264.7 cells with different treatments. (c) Viability of chondrocytes upon incubation with CM of RAW264.7 cells that underwent different treatments. ((d) and (e)) Calcein AM/PI co-staining (d) and apoptosis assay (e) of chondrocytes after exposing to CM of RAW264.7 cells with different treatments (scale bars, 50 μm; data are means ± SD, $n = 3$ (for (a) and (b)) and $n = 6$ (for (c)); ** $p < 0.01$, *** $p < 0.001$, and **** $p < 0.0001$).

(Fig. 4(d)), corroborating the result of CCK-8 test. As confirmed by cell apoptosis analysis, the ratio of healthy chondrocytes in the LPS group was 26.4%, which increased to 55.1% in the LPS + Fe-DexP group (Fig. 4(e)).

2.4 *In vivo* performance of Fe-DexP

Encouraged by the *in vitro* results, the *in vivo* performance of Fe-DexP NPs was evaluated. After local administration of Fe-DexP NPs, significant increase in T_2-weighted MR contrast was observed in knee joint (Fig. 5(a)), demonstrating the feasibility of Fe-DexP NPs for MRI. Next, OA mouse model established by direct injection of papain at the right hind knee joint was used for the investigation of the therapeutic efficacy of Fe-DexP NPs. OA mice were randomly divided into three groups for intra-articular administration of PBS, free DexP, or Fe-DexP NPs. We first detected inflammation-associated ROS at the pathological site with L-012, a bioluminescent probe. As shown in Fig. 5(b) and Fig. S7 in the ESM, bioluminescent signal at knee joints of the PBS group was significantly enhanced compared with that of healthy mice, and was slightly reduced by free DexP. In contrast, Fe-DexP NPs led to striking signal decrease, suggesting its efficacy in amelioration of OA.

Collected knee joints were sectioned and subjected to safranin O/fast green and hematoxylin and eosin (H&E) staining for cartilage histopathological analysis (Figs. 5(c) and 5(d)). Negative safranin O staining, surface abrasion, and inflammatory cells infiltration were observed in the PBS group, indicative of proteoglycan degradation and cartilage destruction which are

characteristics of OA. Free DexP ameliorated cartilage erosion and proteoglycan loss partially, while Fe-DexP NPs treatment resulted in restoration of cartilage surface, absence of inflammatory cells infiltration, and prevention of proteoglycan loss comparable with the healthy mice. Moreover, Osteoarthritis Research Society International (OARSI) score of the Fe-DexP group was significantly lower compared with the PBS group and the free DexP group (Fig. S8 in the ESM) [48]. Taken together, the hybrid NPs could significantly inhibit the OA progression in comparison with DexP. The macrophage phenotypic switch activity of Fe-DexP was further interrogated via immunohistochemical (IHC) staining of M1 and M2 markers in joint sections. As shown in Figs. 5(e) and 5(f), a large amount of pro-inflammatory macrophages (iNOS positive) was observed in the synovial tissue of the PBS group. Free DexP group had the modest impact on the phenotype of macrophages. By comparison, Fe-DexP significantly converted M1-phenotyped macrophages into M2-phenotyped ones, as evidenced by markedly decreased iNOS expression and increased Arg-1 expression. ELISA analysis revealed a significant reduction in the level of intra-articular TNF-α in the Fe-DexP group compared with that in the PBS group (Fig. S9 in the ESM), validating the anti-inflammatory activity of Fe-DexP NPs *in vivo*.

3 Conclusions

In summary, we developed an extremely simple self-assembly approach based on metal-drug coordination to rationally engineer nanohybrids for vehicle-free delivery of anti-inflammatory drugs.
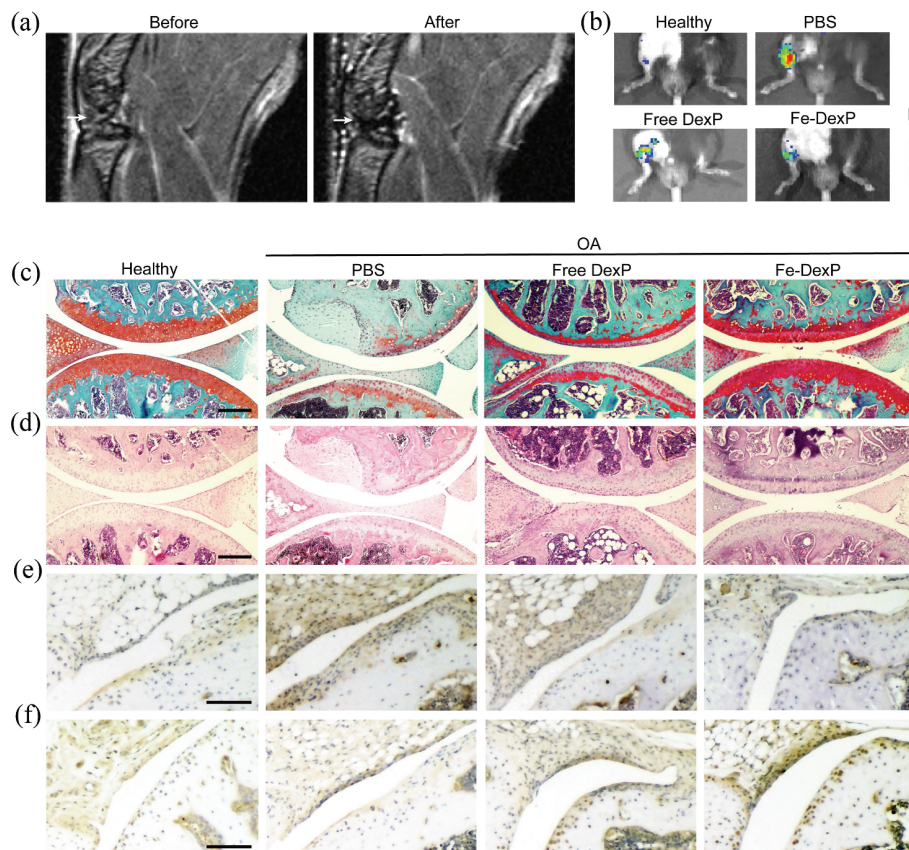
Figure 5 *In vivo* performance of Fe-DexP. (a) *In vivo* T_2-weighted MR images obtained before and after local Fe-DexP injection. Knee articular cavities were indicated by white arrow. (b) Representative *in vivo* luminescence images indicating the inflammatory degree in each group with indicated treatments. ((c) and (d)) Representative Safranin O-fast green (c) and H&E (d) staining images of knee joints from different groups. Scale bars, 100 μm. ((e) and (f)) Representative IHC staining images of iNOS (e) and Arg-1 (f) of the synovial tissue from different groups. Scale bars, 50 μm.

In this manner, potential toxicity of extra synthetic delivery carriers is bypassed. Meanwhile, the resulting metallo-nanodrugs (Fe-DexP) exhibited high drug loading ability as well as stability, which could circumvent the safety issues derived from frequent drug administration. As a result, Fe-DexP renders enhanced anti-inflammatory capacity via re-education of pro-inflammatory M1 macrophages into anti-inflammatory M2 macrophages, suppressing cartilage destruction and ECM degradation in osteoarthritis model. Our work highlights the advantages of leveraging coordination-driven self-assembly strategy to enhance the delivery efficiency and therefore therapeutic efficacy of anti-inflammatory agents.

4   Methods

4.1   Synthesis of Fe-DexP NPs

Fe-DexP NPs were synthesized based on one-pot self-assembly. Typically, 30 μL of an aqueous solution of DexP (20 mM) was added to $FeCl_2 \cdot 4H_2O$ aqueous solution (1.05 mM) and mixed thoroughly. Then hexamethylenetetramine (HMTA) (20 mM, 30 μL) was added into the mixture, followed by 10 s vortex. The solution was incubated at 95 °C for 3 h. After natural cooling, the as-prepared Fe-DexP NPs were centrifuged, washed, and re-dispersed into water for further use.

4.2   *In vitro* and *in vivo* MRI

For *in vitro* MRI, samples of Fe-DexP NPs were prepared in tubes with different concentrations of 0, 0.2, 0.4, 0.6, 0.8, and 1 mM with respect to iron mass. The MR images were collected using spin echo sequence with parameters as follows: repetition time = 3000 ms, echo time = 40 ms, field of view = 35 mm × 35 mm, and

slice thickness = 6/16 mm. The T_2 relaxation times were calculated by fitting these multiple spin echo images. For *in vivo* MRI, mice bearing OA were intra-articularly injected with Fe-DexP NPs (the dose of Fe equivalent to 3.5 mg·kg^{-1}). MR images were taken using a TurboRARE-T_2 sequence with the following parameters: repetition time (TR) = 2500 ms, echo time (TE) = 34.45 ms, matrix = 300 × 300, field of view = 30 mm × 30 mm, slice thickness = 1 mm, and slice number = 20.

4.3   Primary chondrocytes isolation and cell culture

Primary articular chondrocytes were isolated from knee joints and ribs according to previous literature [49]. Briefly, the knee joints and ribs were dislocated with all the soft tissues eliminated. Retrieved cartilage pieces were washed with PBS buffer, then placed in digestion solution containing trypsin (2.5%) for 4 h at 37 °C. Next, the digested samples were treated with type II collagenase (2 mg·mL^{-1}) in 37 °C incubator overnight. The chondrocytes were centrifuged, resuspended in Dulbecco's Modified Eagle Medium (DMEM) supplemented with L-Gln (2 mM), Penicillin G (100 units·mL^{-1}), streptomycin (100 μg·mL^{-1}), and 10% Fetal bovine serum (FBS), and cultured in 37 °C humidified incubator supplement with 5% CO_2. RAW264.7 cells were purchased from Cell Bank of Shanghai Institute of Biochemistry and Cell Biology and cultured in DMEM supplemented with 10% FBS, Penicillin G (100 units·mL^{-1}), streptomycin (100 μg·mL^{-1}), and 1% Glutamine.

4.4   Biosafety assay

RAW264.7 cells were seeded in 96-well plate at a density of 2 × 10^4 cells·well^{-1} and incubated overnight. Afterwards, cells were washed twice with PBS and supplemented with FBS-free DMEM

containing different concentrations of Fe-DexP NPs. After 24 h incubation at 37 °C, cells were washed twice with PBS and supplemented with 100 μL of FBS-free fresh DMEM containing 10% CCK-8 for another 4 h incubation. Absorbance at 450 nm was measured.

4.5 Quantitative analysis of pro-inflammatory cytokines

RAW264.7 cells were cultured in 6-well plates (2×10^5 cells·well^{-1}) beforehand. Then cells were washed twice with PBS and treated with FBS-free DMEM containing LPS (1 μg·mL^{-1}), or LPS (1 μg·mL^{-1}) + Fe-DexP (with the concentration of DexP equivalent to 0, 5, 10, or 20 μg·mL^{-1}), for 24 h. Then the cells were washed twice with PBS and supplemented with fresh FBS-free DMEM. After another 24 h incubation, the supernatant was collected and centrifuged. All samples were stored at −80 °C for ELISA assay of IL-6 and TNF-α under manufacturer's instructions.

4.6 Intracellular ROS measurement

Intracellular ROS was measured by both confocal laser scanning microscopy (CLSM) imaging and flow cytometry analysis. RAW264.7 seeded beforehand were washed and incubated in FBS-free DMEM containing LPS (1 μg·mL^{-1}) and Fe-DexP (with the concentration of DexP equivalent to 0, 5, 10, or 20 μg·mL^{-1}). After further incubation for 6 h, cells were washed twice and supplemented with FBS-free DMEM containing 10 μM DCFH-DA for another 20 min incubation. Then treated cells were washed for CLSM imaging or flow cytometry analysis.

4.7 Western blot assay

RAW264.7 cells were grown in 6-well plates overnight. After treatment with LPS (1 μg·mL^{-1}) and Fe-DexP (with the concentration of DexP equivalent to 20 μg·mL^{-1}), total protein was extracted by RIPA lysis buffer containing 1 mM phenylmethylsulfonyl fluoride (PMSF; Beyotime, ST506). After centrifuging at 12,000 g at 4 °C for 15 min, the supernatant was collected. The protein concentration was determined by using a bicinchoninic acid (BCA) Protein Assay Kit (Nanjing Jiancheng Bioengineering Institute, A045-4). The protein samples were separated by 10% sodium dodecyl sulphate-polyacrylamide gel electrophoresis (SDS-PAGE) before transferred onto polyvinylidene fluoride (PVDF) membrane (Millipore, 0.22 μm). After blocking in 5% nonfat dried milk diluted by Tris-buffered saline with 0.05% Tween (TBST, 25 mM Tris, 0.15 M NaCl, and 0.05% Tween-20) for 1.5 h, membranes were incubated with anti-COX-2 antibody (HuaBio, ET1610-23, dilution 1:1000) and β-actin monoclonal antibody (Transgen, HC201-01, dilution 1:1000) followed by peroxidase-conjugated anti-rabbit IgG (Transgen, dilution 1:1000) and anti-mouse IgG (Transgen, dilution 1:1000). Images were obtained on a chemiluminescence system.

4.8 q-PCR assay

RAW264.7 cells were grown in 6-well plate beforehand. Then cells were treated same as in western blot assay. Next, total RNA was extracted with TRIzol reagent (Invitrogen, Ambion) in RNase-free condition and reverse transcribed into cDNA with a reverse transcription kit (Transgen, China) under the instructions of the manufacturer. q-PCR was performed with SYBR Green PCR kit (TransStart® Green qPCR SuperMix, China) on the Applied Biosystems (USA) to determine gene expression level. The q-PCR running conditions were as follows: 94 °C for 3 min; and 40 cycles of 94 °C for 10 s, 60 °C for 20 s, and 72 °C for 20 s. Expression was normalized to the β-actin housekeeping gene and calculated with the comparative method ($2^{-\Delta\Delta Ct}$). All the primer sequences used in the study are listed in Table S1 in the ESM.

4.9 Cell viability and apoptosis test of chondrocytes

Chondrocytes were cultured in 96-well plate or 6-well plate at 2×10^4 cells·well^{-1} and incubated overnight to allow the confluence to reach 70%–80%. Then the chondrocytes were washed and supplemented with CM of RAW24.7 cells treated with LPS (1 μg·mL^{-1}) or LPS (1 μg·mL^{-1}) + Fe-DexP NPs (with the concentration of DexP equivalent to 20 μg·mL^{-1}), followed by 24 h incubation. For cell viability assay, fresh FBS-free DMEM containing 10% CCK-8 was added for another 4 h incubation, with the absorbance at 450 nm measured. For apoptosis assay, the chondrocytes were collected and stained with Annexin V and PI using Annexin V-APC/PI apoptosis detection kit, followed by flow cytometry analysis.

4.10 Live/dead cell co-staining

Chondrocytes cultured beforehand were incubated with CM of RAW24.7 cells treated with LPS (1 μg·mL^{-1}) or LPS (1 μg·mL^{-1}) + Fe-DexP NPs (with the concentration of DexP equivalent to 20 μg·mL^{-1}). After 24 h incubation, chondrocytes were stained with Calcein-AM/PI double staining kit according to the instructions of manufacturer and trypsinized for CLSM imaging.

4.11 Animal model

The animal study protocol was approved by the Institutional Animal Care and Use Committee of National Center for Nanoscience and Technology (Ethics No. NCNST21-22060403). Male C57BL/6J mice (8 weeks old, 18–20 g) were supplied by Beijing Vital River Laboratory Animal Technology Co., Ltd. To establish OA model, 20 μL aqueous solution of papain (0.8%) and L-cysteine (0.03 M) were intra-articularly injected into right knee joint of mice every 3 days for three times.

4.12 Osteoarthritis therapy

OA mice were treated with free DexP (1.5 mg·kg^{-1}) or Fe-DexP (3.0 mg·kg^{-1}) intra-articularly every 4 days for a total of four times. Healthy mice without OA model establishment were set as control. At end of the study, all mice were euthanized with the knee joints collected, fixed with 4% paraformaldehyde, and decalcified with ethylenediaminetetraacetate (EDTA) for 2 weeks. The specimens were dehydrated for paraffin-embedded and sectioned to 4 μm for H&E, Safranin O/Fast Green, and immunohistochemical staining. The osteoarthritis severity degree was evaluated according to the OARSI scoring system [48]. For measurement of TNF-α, knee joint tissue was homogenized and centrifuged, with the supernatant collected for ELISA assay.

4.13 *In vivo* luminescence imaging

At the end of treatment, L-012 probe (75 mg·kg^{-1}) was subcutaneously delivered to inflamed joint, and the luminescence images of the inflamed knees were then obtained using an *in vivo* imaging system (IVIS) imaging system.

4.14 Statistical analysis

Statistical evaluation was carried out using GraphPad Prism 8 software. The difference between two groups was compared using the Student's *t* test, "*P*" values < 0.05 were considered statistically different (*$p < 0.05$, **$p < 0.01$, ***$p < 0.001$, and ****$p < 0.0001$).

Acknowledgements

References

[1] Medzhitov, R. Origin and physiological roles of inflammation. *Nature* **2008**, *454*, 428–435.

[2] Wieland, H. A.; Michaelis, M.; Kirschbaum, B. J.; Rudolphi, K. A. Osteoarthritis-an untreatable disease. *Nat. Rev. Drug Discov.* **2005**, *4*, 331–344.

[3] Latourte, A.; Kloppenburg, M.; Richette, P. Emerging pharmaceutical therapies for osteoarthritis. *Nat. Rev. Rheumatol.* **2020**, *16*, 673–688.

[4] Liu-Bryan, R.; Terkeltaub, R. Emerging regulators of the inflammatory process in osteoarthritis. *Nat. Rev. Rheumatol.* **2015**, *11*, 35–44.

[5] McAlindon, T. E.; LaValley, M. P.; Harvey, W. F.; Price, L. L.; Driban, J. B.; Zhang, M.; Ward, R. J. Effect of intra-articular triamcinolone vs saline on knee cartilage volume and pain in patients with knee osteoarthritis. *JAMA* **2017**, *317*, 1967–1975.

[6] Evans, C. H.; Kraus, V. B.; Setton, L. A. Progress in intra-articular therapy. *Nat. Rev. Rheumatol.* **2014**, *10*, 11–22.

[7] Larsen, C.; Østergaard, J.; Larsen, S. W.; Jensen, H.; Jacobsen, S.; Lindegaard, C.; Andersen, P. H. Intra-articular depot formulation principles: Role in the management of postoperative pain and arthritic disorders. *J. Pharm. Sci.* **2008**, *97*, 4622–4654.

[8] Rosen, H.; Abribat, T. The rise and rise of drug delivery. *Nat. Rev. Drug Discov.* **2005**, *4*, 381–385.

[9] Williams, R. M.; Chen, S.; Langenbacher, R. E.; Galassi, T. V.; Harvey, J. D.; Jena, P. V.; Budhathoki-Uprety, J.; Luo, M. K.; Heller, D. A. Harnessing nanotechnology to expand the toolbox of chemical biology. *Nat. Chem. Biol.* **2021**, *17*, 129–137.

[10] Datta, S.; Saha, M. L.; Stang, P. J. Hierarchical assemblies of supramolecular coordination complexes. *Acc. Chem. Res.* **2018**, *51*, 2047–2063.

[11] Furukawa, H.; Cordova, K. E.; O'Keeffe, M.; Yaghi, O. M. The chemistry and applications of metal–organic frameworks. *Science* **2013**, *341*, 1230444.

[12] Foo, M. L.; Matsuda, R.; Kitagawa, S. Functional hybrid porous coordination polymers. *Chem. Mater.* **2014**, *26*, 310–322.

[13] Liu, M. J.; Ren, X. L.; Meng, X. W.; Li, H. B. Metal–organic frameworks-based fluorescent nanocomposites for bioimaging in living cells and *in vivo*. *Chin. J. Chem.* **2021**, *39*, 473–487.

[14] He, C. B.; Liu, D. M.; Lin, W. B. Nanomedicine applications of hybrid nanomaterials built from metal-ligand coordination bonds: Nanoscale metal–organic frameworks and nanoscale coordination polymers. *Chem. Rev.* **2015**, *115*, 11079–11108.

[15] Zhou, J. J.; Han, H. Y.; Liu, J. W. Nucleobase, nucleoside, nucleotide, and oligonucleotide coordinated metal ions for sensing and biomedicine applications. *Nano Res.* **2022**, *15*, 71–84.

[16] Zhang, Z.; Li, B.; Xie, L. S.; Sang, W.; Tian, H.; Li, J.; Wang, G. H.; Dai, Y. L. Metal–phenolic network-enabled lactic acid consumption reverses immunosuppressive tumor microenvironment for sonodynamic therapy. *ACS Nano* **2021**, *15*, 16934–16945.

[17] Imaz, I.; Rubio-Martínez, M.; García-Fernández, L.; García, F.; Ruiz-Molina, D.; Hernando, J.; Puntes, V.; Maspoch, D. Coordination polymer particles as potential drug delivery systems. *Chem. Commun.* **2010**, *46*, 4737–4739.

[18] Horcajada, P.; Gref, R.; Baati, T.; Allan, P. K.; Maurin, G.; Couvreur, P.; Férey, G.; Morris, R. E.; Serre, C. Metal–organic frameworks in biomedicine. *Chem. Rev.* **2012**, *112*, 1232–1268.

[19] Wang, D. D.; Jana, D.; Zhao, Y. L. Metal–organic framework derived nanozymes in biomedicine. *Acc. Chem. Res.* **2020**, *53*, 1389–1400.

[20] Taylor-Pashow, K. M. L.; Rocca, J. D.; Xie, Z. G.; Tran, S.; Lin W. B. Postsynthetic modifications of iron-carboxylate nanoscale metal-organic frameworks for imaging and drug delivery. *J. Am. Chem. Soc.* **2009**, *131*, 14261–14263.

[21] Zheng, H. Q.; Zhang, Y. N.; Liu, L. F.; Wan, W.; Guo, P.; Nyström, A. M.; Zou, X. D. One-pot synthesis of metal–organic frameworks with encapsulated target molecules and their applications for controlled drug delivery. *J. Am. Chem. Soc.* **2016**, *138*, 962–968.

[22] Wang, P.; Zhou, F.; Yin, X.; Xie, Q. J.; Song, G. S.; Zhang, X. B. Nanovoid-confinement and click-activated nanoreactor for synchronous delivery of prodrug pairs and precise photodynamic therapy. *Nano Res.* **2022**, *15*, 9264–9273.

[23] Ma, Y.; Li, X. Y.; Li, A. J.; Yang, P.; Zhang, C. Y.; Tang, B. H$_2$S-activable MOF nanoparticle photosensitizer for effective photodynamic therapy against cancer with controllable singlet-oxygen release. *Angew. Chem., Int. Ed.* **2017**, *56*, 13752–13756.

[24] Zhang, P. F.; Wang, J. Q.; Chen, H.; Zhao, L.; Chen, B. B.; Chu, C. C.; Liu, H.; Qin, Z. N.; Liu, J. Y.; Tan, Y. Z. et al. Tumor microenvironment-responsive ultrasmall nanodrug generators with enhanced tumor delivery and penetration. *J. Am. Chem. Soc.* **2018**, *140*, 14980–14989.

[25] Hu, J. L.; Jiang, Q. Y.; Shi, T. H.; Lin, X.; Zhao, Y.; Wang, X. Y.; Liu, X. Q. *In situ* generated and amplified oxidative stress with metallo-nanodrug assembly for metastatic cancer therapy with high specificity and efficacy. *Adv. Therap.* **2021**, *4*, 2100148.

[26] Zhu, W. J.; Chen, Q.; Jin, Q. T.; Chao, Y.; Sun, L. L.; Han, X.; Xu, J.; Tian, L. L.; Zhang, J. L.; Liu, T. et al. Sonodynamic therapy with immune modulatable two-dimensional coordination nanosheets for enhanced anti-tumor immunotherapy. *Nano Res.* **2021**, *14*, 212–221.

[27] Cheng, K.; Liu, B.; Zhang, X. S.; Zhang, R. Y.; Zhang, F.; Ashraf, G.; Fan, G. Q.; Tian, M. Y.; Sun, X.; Yuan, J. et al. Biomimetic material degradation for synergistic enhanced therapy by regulating endogenous energy metabolism imaging under hypothermia. *Nat. Commun.* **2022**, *13*, 4567.

[28] Luo, Z. C.; Liang, X. Q.; He, T.; Qin, X.; Li, X. C.; Li, Y. S.; Li, L.; Loh, X. J.; Gong, C. Y.; Liu, X. G. Lanthanide-nucleotide coordination nanoparticles for STING activation. *J. Am. Chem. Soc.* **2022**, *144*, 16366–16377.

[29] Zhou, H. S.; Wang, Y. Y.; Hou, Y. Q.; Zhang, Z. K.; Wang, Q.; Tian, X. D.; Lu, H. Co-delivery of Cisplatin and chlorin e6 by poly(phosphotyrosine) for synergistic chemotherapy and photodynamic therapy. *Chin. J. Chem.* **2022**, *40*, 2428–2436.

[30] Li, M. Y.; Wang, C. L.; Di, Z. H.; Li, H.; Zhang, J. F.; Xue, W. T.; Zhao, M. P.; Zhang, K.; Zhao, Y. L.; Li, L. L. Engineering multifunctional DNA hybrid nanospheres through coordination-driven self-assembly. *Angew. Chem., Int. Ed.* **2019**, *58*, 1350–1354.

[31] Liu, B.; Hu, F.; Zhang, J. F.; Wang, C. L.; Li, L. L. A biomimetic coordination nanoplatform for controlled encapsulation and delivery of drug-gene combinations. *Angew. Chem., Int. Ed.* **2019**, *58*, 8804–8808.

[32] Liu, C. Z.; Chen, Y. X.; Zhao, J.; Wang, Y.; Shao, Y. L.; Gu, Z. J.; Li, L. L.; Zhao, Y. L. Self-assembly of copper-DNAzyme nanohybrids for dual-catalytic tumor therapy. *Angew. Chem., Int. Ed.* **2021**, *60*, 14324–14328.

[33] Zou, Z.; He, L. B.; Deng, X. X.; Wang, H. X.; Huang, Z. Y.; Xue, Q.; Qing, Z. H.; Lei, Y. L.; Yang, R. H.; Liu, J. W. Zn^{2+}-coordination-driven RNA assembly with retained integrity and biological functions. *Angew. Chem., Int. Ed.* **2021**, *60*, 22970–22976.

[34] Dubashynskaya, N. V.; Bokatyi, A. N.; Skorik, Y. A. Dexamethasone conjugates: Synthetic approaches and medical prospects. *Biomedicines* **2021**, *9*, 341.

[35] Yamashita, T.; Hayes, P. Analysis of XPS spectra of Fe^{2+} and Fe^{3+} ions in oxide materials. *Appl. Surf. Sci.* **2008**, *254*, 2441–2449.

[36] Pan, Q.; Xu, Q. G.; Boylan, N. J.; Lamb, N. W.; Emmert, D. G.; Yang, J. C.; Tang, L.; Heflin, T.; Alwadani, S.; Eberhart, C. G. et al. Corticosteroid-loaded biodegradable nanoparticles for prevention of corneal allograft rejection in rats. *J. Control. Release* **2015**, *201*, 32–40.

[37] Muhammad, W.; Zhu, J. Q.; Zhai, Z. H.; Xie, J. Q.; Zhou, J. H.; Feng, X. D.; Feng, B.; Pan, Q. L.; Li, S. F.; Venkatesan, R. J. et al. ROS-responsive polymer nanoparticles with enhanced loading of dexamethasone effectively modulate the lung injury microenvironment. *Acta Biomater.* **2022**, *148*, 258–270.

[38] Chen, Y. J.; Li, P.; Modica, J. A.; Drout, R. J.; Farha, O. K. Acid-resistant mesoporous metal–organic framework toward oral insulin

delivery: Protein encapsulation, protection, and release. *J. Am. Chem. Soc.* **2018**, *140*, 5678–5681.

[39] Lu, Y. C.; Yeh, W. C.; Ohashi, P. S. LPS/TLR4 signal transduction pathway. *Cytokine* **2008**, *42*, 145–151.

[40] Bode, J. G.; Ehlting, C.; Häussinger, D. The macrophage response towards LPS and its control through the p38^{MAPK}-STAT3 axis. *Cell. Signal.* **2012**, *24*, 1185–1194.

[41] Gilroy, D. W.; Colville-Nash, P. R. New insights into the role of COX 2 in inflammation. *J. Mol. Med.* **2000**, *78*, 121–129.

[42] Zhao, C. Y.; Chen, J. X.; Ye, J. M.; Li, Z.; Su, L. C.; Wang, J. Q.; Zhang, Y.; Chen, J. H.; Yang, H. H.; Shi, J. J. et al. Structural transformative antioxidants for dual-responsive anti-inflammatory delivery and photoacoustic inflammation imaging. *Angew. Chem., Int. Ed.* **2021**, *60*, 14458–14466.

[43] Mittal, M.; Siddiqui, M. R.; Tran, K.; Reddy, S. P.; Malik, A. B. Reactive oxygen species in inflammation and tissue injury. *Antioxid. Redox Signal.* **2014**, *20*, 1126–1167.

[44] Zhao, P. C.; Xia, X. F.; Xu, X. Y.; Leung, K. K. C.; Rai, A.; Deng, Y. R.; Yang, B. G.; Lai, H. S.; Peng, X.; Shi, P. et al. Nanoparticle-assembled bioadhesive coacervate coating with prolonged gastrointestinal retention for inflammatory bowel disease therapy. *Nat. Commun.* **2021**, *12*, 7162.

[45] Jiang, K. Y.; Weaver, J. D.; Li, Y. J. Y.; Chen, X. J.; Liang, J. P.; Stabler, C. L. Local release of dexamethasone from macroporous scaffolds accelerates islet transplant engraftment by promotion of anti-inflammatory M2 macrophages. *Biomaterials* **2017**, *114*, 71–81.

[46] Loeser, R. F. Molecular mechanisms of cartilage destruction: Mechanics, inflammatory mediators, and aging collide. *Arthrit. Rheumatol.* **2016**, *54*, 1357–1360.

[47] Li, M. Z.; Yin, H.; Yan, Z. N.; Li, H. Y.; Wu, J.; Wang, Y.; Wei, F.; Tian, G. Z.; Ning, C.; Li, H. et al. The immune microenvironment in cartilage injury and repair. *Acta Biomater.* **2022**, *140*, 23–42.

[48] Glasson, S. S.; Chambers, M. G.; Van Den Berg, W. B.; Little, C. B. The OARSI histopathology initiative-recommendations for histological assessments of osteoarthritis in the mouse. *Osteoarthritis Cartilage* **2010**, *18 Suppl 3*, S17–S23.

[49] Chen, H. M.; Qin, Z. N.; Zhao, J. M.; He, Y.; Ren, E.; Zhu, Y.; Liu, G.; Mao, C. B.; Zheng, L. Cartilage-targeting and dual MMP-13/pH responsive theranostic nanoprobes for osteoarthritis imaging and precision therapy. *Biomaterials* **2019**, *225*, 119520.